Golden-Angle Radial Sparse Parallel MRI: Combination of Compressed Sensing, Parallel Imaging, and Golden-Angle Radial Sampling for Fast and Flexible Dynamic Volumetric MRI

Li Feng,[1,2]* Robert Grimm,[3] Kai Tobias Block,[1] Hersh Chandarana,[1] Sungheon Kim,[1,2] Jian Xu,[4] Leon Axel,[1,2] Daniel K. Sodickson,[1,2] and Ricardo Otazo[1,2]

Purpose: To develop a fast and flexible free-breathing dynamic volumetric MRI technique, iterative Golden-angle RAdial Sparse Parallel MRI (iGRASP), that combines compressed sensing, parallel imaging, and golden-angle radial sampling.
Methods: Radial k-space data are acquired continuously using the golden-angle scheme and sorted into time series by grouping an arbitrary number of consecutive spokes into temporal frames. An iterative reconstruction procedure is then performed on the undersampled time series where joint multicoil sparsity is enforced by applying a total-variation constraint along the temporal dimension. Required coil-sensitivity profiles are obtained from the time-averaged data.
Results: iGRASP achieved higher acceleration capability than either parallel imaging or coil-by-coil compressed sensing alone. It enabled dynamic volumetric imaging with high spatial and temporal resolution for various clinical applications, including free-breathing dynamic contrast-enhanced imaging in the abdomen of both adult and pediatric patients, and in the breast and neck of adult patients.
Conclusion: The high performance and flexibility provided by iGRASP can improve clinical studies that require robustness to motion and simultaneous high spatial and temporal resolution.
Magn Reson Med 000:000–000, 2013. © 2013 Wiley Periodicals, Inc.

Key words: compressed sensing; parallel imaging; radial sampling; golden-angle; joint sparsity; dynamic imaging

INTRODUCTION

Dynamic MRI requires rapid data acquisition to provide an appropriate combination of spatial resolution, temporal resolution, and volumetric coverage for clinical studies. For example, rapid imaging speed is needed for dynamic contrast-enhanced (DCE) examinations, in which fast signal-intensity changes must be monitored during the passage of the contrast agent (1,2). A variety of fast MRI techniques have been developed to accelerate the data acquisition. Parallel imaging (PI) techniques, such as SMASH (3), SENSE (4), and GRAPPA (5), use spatial information from multiple receiver coils with different sensitivity patterns to reconstruct images from undersampled multicoil data. Temporal PI techniques, such as TSENSE (6) or TGRAPPA (7), remove the need to acquire extra coil reference data, by combining different temporal frames acquired with shifted undersampling patterns. However, the acceleration in PI is limited by SNR constraints and restrictions in the coil design, which can result in a poorly conditioned inverse problem for high accelerations. The presence of extensive spatial and temporal correlations can be also exploited to accelerate the data acquisition (8). The k-t acceleration methods, such as k-t BLAST/k-t SENSE (9), k-t GRAPPA (10), and SPEAR (11), are based on the fact that the representation of dynamic images in the combined spatial (x) and temporal Fourier (f) domain is typically sparse, which reduces the signal aliasing in x-f space due to regular k-t undersampling and makes higher accelerations feasible. Other techniques, such as keyhole imaging (12) or TRICKS (13), aim to accelerate data acquisition and increase temporal resolution by sharing portions of the k-space data.

Compressed sensing (CS) (14–16) is another strategy to accelerate data acquisition in dynamic MRI. CS methods exploit spatial and temporal correlations by using irregular undersampling schemes to create incoherent aliasing artifacts and using a nonlinear reconstruction to enforce sparsity in a suitable transform domain (17–24). Incoherent aliasing artifacts are often created using Cartesian k-space trajectories with random undersampling patterns (16). However, the incoherence achievable in this way is relatively low, which limits the performance of CS. Radial k-space trajectories (25,26) are an interesting alternative due to the inherent presence of incoherent aliasing in multiple dimensions (25), even for regular (nonrandom) undersampling. Moreover, radial trajectories are less sensitive to motion, which improves capturing dynamic information (26,27). When acquiring radial data according to the golden-angle ordering scheme (28),

where the angle of the radial lines is increased continuously by 111.25°, a rather uniform coverage of k-space with high temporal incoherence is obtained for any arbitrary number of consecutive lines. This enables dynamic imaging studies using continuous data acquisition and retrospective reconstruction of image series with arbitrary temporal resolution by grouping different numbers of consecutive radial lines into temporal frames (29,30). Higher accelerations can be achieved by combining CS and PI using the idea of joint multicoil sparsity, as previously demonstrated for accelerated dynamic MRI in Cartesian k-space trajectories with the k-t SPARSE-SENSE technique (21–24).

In this work, the idea of k-t SPARSE-SENSE is extended to volumetric golden-angle radial acquisitions and demonstrated for various clinical dynamic imaging applications, including free-breathing liver DCE MRI, pediatric body MRI, breast and neck imaging. The performance of the extended approach, entitled iterative Golden-angle RAdial Sparse Parallel MRI (iGRASP), is compared with coil-by-coil CS and PI-only reconstructions.

METHODS

Golden-Angle Radial Sampling

Continuous 3D data acquisition was implemented using a stack-of-stars k-space trajectory, where Cartesian sampling is used along the partition dimension (k_z) and golden-angle radial sampling is used in the k_x-k_y plane, as summarized in Figure 1a. The golden-angle acquisition scheme, which has previously been applied for accelerated dynamic imaging (30–32), ensures approximately uniform coverage of k-space for any arbitrary number of consecutive spokes, in particular if the number belongs to the Fibonacci series [defined as $F(k+2) = F(k) + F(k+1)$, where $k \geq 0$, and $F(0) = 0$ and $F(1) = 1$, e.g., 1,2,3,5,8,13,21,34,...] (28). Figure 1b shows the point spread function (PSF) for a golden-angle radial acquisition with 21 spokes using a single element receiver coil (top) and a sensitivity-weighted combination of eight radiofrequency (RF) coil elements (bottom). The PSF for the single coil is calculated by performing gridding on a simulated k-space matrix with ones along an undersampled radial trajectory with 21 golden-angle spokes and 256 sampling points along each spoke, followed by an inverse nonuniform fast Fourier transform (NUFFT) operation. The Nyquist sampling requirement for this case is $256*\pi/2 \approx 402$, corresponding to a simulated acceleration rate of 19.1. The PSF is indicative of the degree of incoherence associated with the radial undersampling before the compressed-sensing reconstruction. The PSF of the eight-coil acquisition with identical acceleration was computed using the multicoil SENSE model, which performs a sensitivity-weighted combination of individual PSFs using simulated sensitivity maps. The resulting incoherence, which was computed as the ratio of the main-lobe to the standard deviation of the side-lobes in the PSF (16), was 83.1 for the single-coil case and 106.9 for the eight-coil case. As shown in the Figure 1b, the use of the multicoil SENSE model reduces the side-lobes, which correspond to aliasing artifacts due to undersampling. The higher encoding capabilities provided by the coil array therefore improve the performance of compressed sensing (21).
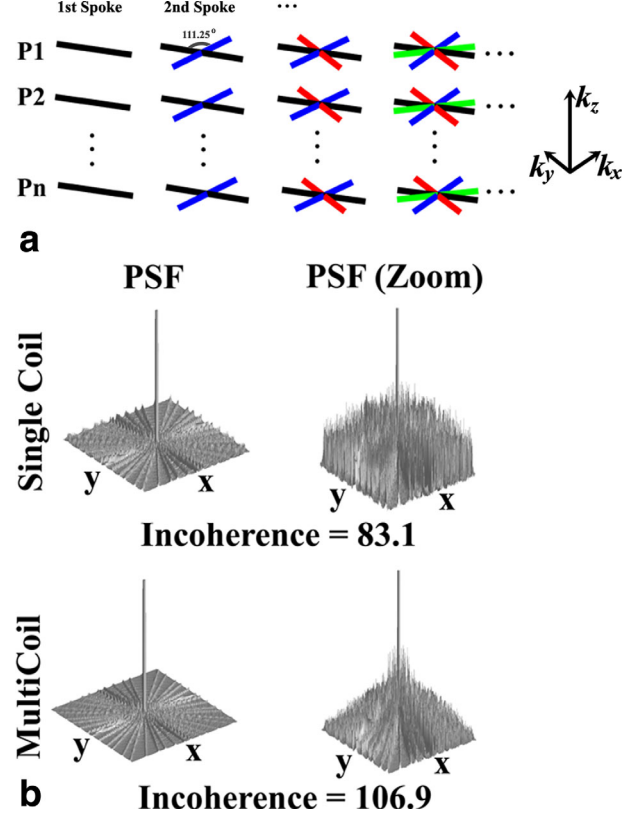

FIG. 1. **a**: Continuous acquisition of radial lines with stack-of-stars golden-angle scheme in iGRASP. **b**: Point spread function (PSF) of an undersampled radial trajectory with 21 golden-angle spokes and 256 sampling points in each readout spoke for a single element coil (top) and for a sensitivity-weighted combination of eight RF coil elements (bottom). The Nyquist sampling requirement is $256*\pi/2 \approx 402$. The standard deviation of the PSF side lobes was used to quantify the power of the resulting incoherent artifacts (pseudo-noise) and incoherence was computed using the main-lobe to pseudo-noise ratio of the PSF.

iGRASP Reconstruction

Figure 2 shows the iGRASP reconstruction pipeline. Because the k_z dimension is uniformly sampled, a fast Fourier transform (FFT) is applied along this dimension to enable slice-by-slice reconstructions, which reduces the computational burden and enables straightforward parallelization of the reconstruction. Coil sensitivity maps are computed with the adaptive array-combination technique (33,34) using coil-reference data from the temporal average of all acquired spokes, which is usually fully sampled as shown in Figure 2a. Afterward, the continuously acquired radial spokes are re-sorted by grouping a Fibonacci number (e.g., 34, 21, or 13) of consecutive spokes to form each temporal frame with the desired temporal resolution. The iGRASP reconstruction is formulated as follows:
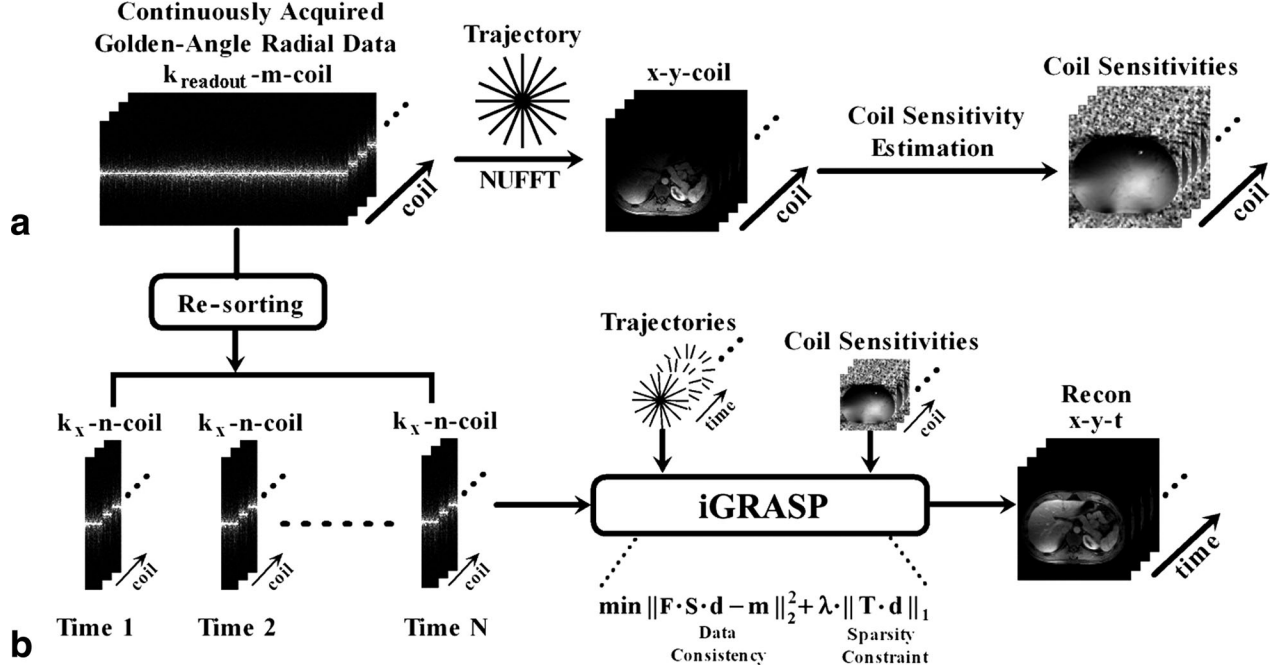
FIG. 2. iGRASP reconstruction pipeline. **a:** Estimation of coil sensitivity maps in the image domain, where the multicoil reference image (x-y-coil) is given by the coil-by-coil NUFFT reconstruction of the composite k-space data set that results from grouping all the acquired spokes. **b:** Reconstruction of the image time-series, where the continuously acquired data are first re-sorted into undersampled dynamic time series by grouping several consecutive spokes. The iGRASP reconstruction algorithm is then applied to the re-sorted multicoil radial data, using the NUFFT and the coil sensitivities to produce the unaliased image time-series (x-y-t).

$$\hat{d} = \arg\min\{\| F \cdot S \cdot d - m \|_2^2 + \lambda \| T \cdot d \|_1\}, \qquad [1]$$

where **d** is the image series to be reconstructed in *x-y-t* space, **T** is the temporal total-variation (TV) operator (sparsifying transform), imposed on the l_1 norm, m = $\begin{bmatrix} m_1 \\ \vdots \\ m_c \end{bmatrix}$ are the acquired multicoil radial k-space data with c coils, **F** is the NUFFT operator defined on the radial acquisition pattern, S = $\begin{bmatrix} S_1 \\ \vdots \\ S_c \end{bmatrix}$ are the coil sensitivity maps in *x-y* space, and λ is the regularization weight that controls the tradeoff between parallel-imaging data consistency and sparsity. A ramp filter in the k_x-k_y plane was applied to each spoke to compensate for variable density sampling.

Selection of Reconstruction Parameters

To determine the optimal weighting parameter λ, the performance of several values was first evaluated on one dataset for one temporal resolution and then adjusted for other temporal resolutions according to the difference in aliasing artifacts (pseudo-noise). First, iGRASP reconstructions were performed using different weights ranging from 0.01* M_0 to 0.1* M_0 (step size 0.01), where M_0 was the maximal magnitude value of the NUFFT images that are also used to initialize the iGRASP reconstruction, for the case of 21 spokes per temporal frame. An

adequate value for λ was chosen by an experienced radiologist, who identified the appropriate value corresponding to the adequate balance between preservation of fine detail and residual noise or pseudo-noise level, and who also evaluated the signal intensity of regions of interest (ROIs) along time. The parameter for different temporal resolutions was then obtained with A_t/A_{21} * λ_{21}, where A_t is the pseudo-noise at the target temporal resolution and A_{21} is the pseudo-noise at 21 spokes per frame. The pseudo-noise was computed as described before. In this way, higher temporal resolutions (or equivalently, use of fewer spokes for each temporal frame) will be regularized more strongly, proportionally to the higher level of pseudo-noise. This parameter estimation procedure needs to be performed only once for a certain target temporal resolution and application area (liver imaging in this work), and the value can then be used for different temporal resolutions and applications.

Implementation of the Reconstruction Algorithm

The iGRASP reconstruction was initially implemented in a customized software developed in MATLAB (Mathworks, MA), using a tailored version of the nonlinear conjugate gradient algorithm originally proposed in (16). The reconstruction code is available online at http://cai2r.net/resources/software/grasp-matlab-code.

To achieve reconstruction times that allow for more practical evaluation in clinical settings, the reconstruction was also implemented as a stand-alone application using the C++ language. Several algorithmic optimizations were incorporated to achieve high reconstruction speed. First, a channel-compression procedure was

Table 1
Representative Imaging Parameters Of Dynamic Volumetric MRI In Different Applications

	DCE Liver	DCE Pediatrics	DCE Breast	DCE Neck
#Sampling in Each Readout (2×)	512∼768	512	512	512
#Partitions	29∼40	48	35	69
#Spokes in Each Partition	600∼800	800	2280	800
Slice Thickness (mm)	3	3	2	2
FOV (mm^2)	370×370	250×250	270×270	256×256
TR/TE (ms)	3.83/1.71	4.24/2.07	3.6/1.47	4.57/2.06
Flip Angle (Degree)	12	12	12	12
Acquisition Time (s)	90	193	331	283

applied to reduce the amount of k-space data, which combined the receiver channels into eigenmodes based on a principal component analysis and discarded higher-order modes such that 95% of the signal power was preserved (35). Second, the reconstruction was parallelized across slices using the OpenMP framework (36), yielding an almost linear reduction of the reconstruction time with the number of processor cores. The NUFFT was implemented by means of convolution with a Kaiser-Bessel kernel. Interpolation coefficients were precalculated and shared across threads. Corner rounding was applied to allow for differentiation of the TV l_1 norm. Minimization of the cost function was achieved with a C implementation of the limited-memory Broyden-Fletcher-Goldfarb-Shanno (L-BFGS) algorithm (37).

Representative Imaging Applications

iGRASP dynamic imaging was clinically implemented and evaluated for a variety of representative imaging applications, as described in the following subsections. Human imaging was approved by institutional review board and was Health Insurance Portability and Accountability Act (HIPAA) compliant. Written informed consent was obtained from all the subjects before the imaging.

Dynamic Contrast-Enhanced Liver Imaging

DCE liver MRI was performed in six healthy volunteers (age, 34.5 ± 5.2 years) and seven patients (age, 51 ± 8.4 years) in axial orientation during free breathing using whole-body 3 Tesla (T) or 1.5T scanners (MAGNETOM Verio / Avanto, Siemens AG, Erlangen, Germany) with a combination of body-matrix and spine coil elements with 12 channels in total. Data acquisition was initiated simultaneously with intravenous injection of 10 mL of gadopentate dimeglumine (Gd-DTPA) (Magnevist, Bayer Healthcare, Leverkusen) followed by a 20-mL saline flush, both injected at a rate of 2 mL/s. A radial stack-of-stars three-dimensional (3D) Fast Low Angle SHot (FLASH) pulse sequence with golden-angle ordering was employed for the data acquisitions. Two-fold readout oversampling was applied to avoid spurious aliasing along the spokes. All partitions corresponding to one radial angle were acquired sequentially before moving to the next angle. The ordering scheme along kz was switched between linear (from $kz=-kzmax/2$ to $kz=+kzmax/2$) and centric out (starting at $kz=0$) depend-

ing on the number of slices, as done in most of the modern 3D gradient echo (GRE) sequences. Frequency-selective fat suppression was used and 60 initial calibration lines were acquired to correct system-dependent gradient-delay errors as described by Block and Uecker (38). Relevant imaging parameters are listed in Table 1.

Dynamic Contrast-Enhanced Pediatric Body Imaging

Abdominal DCE MRI was performed in five pediatric patients (age 4.8 ± 4.1 years) in axial orientation on a 1.5T scanner (MAGNETOM Avanto, Siemens AG) using a body/spine coil array with 12 elements. Acquisitions were performed during free-breathing because the patients were sedated during the exam. The imaging and contrast-injection protocols were comparable to the liver example described above. Relevant parameters are listed in Table 1.

Dynamic Contrast-Enhanced Breast Imaging

Free-breathing unilateral breast DCE MRI was performed in six patients (age, 55.3 ± 6.7 years) in sagittal orientation before MRI-guided biopsy using the radial 3D FLASH protocol on a 3T scanner (MAGNETOM Trio, Siemens AG), equipped with a seven-element breast-coil array (InVivo Corporation, Gainesville, FL). A single dose of Gd-DTPA with concentration of 0.1 mM/kg body weight was injected at 3 mL/s into an antecubital vein. Relevant imaging parameters are listed in Table 1.

Dynamic Contrast-Enhanced Neck Imaging

DCE MRI of the neck was performed in 10 patients (age, 66.2 ± 19.9 years) in axial orientation using the radial 3D FLASH protocol on a 1.5T scanner (MAGNETOM Avanto, Siemens AG), using a head/spine coil with 15 elements. The contrast-injection protocol was identical to the liver example. Relevant imaging parameters are listed in Table 1.

Image Reconstruction

Iterative SENSE, coil-by-coil CS, and iGRASP reconstructions were performed on all the datasets using 21 spokes for each temporal frame. The reconstructed in-plane matrix size was 256 × 256 or 384 × 384, depending on the number of readout samples. The achieved temporal resolution was approximately 3 s/volume for the liver application, 5 s/volume for the pediatric application,

3 s/volume for breast imaging and 7 s/volume for neck imaging. Compared with the Nyquist sampling rate, the reconstructions correspond to an acceleration rate of 19.1 to 28.7.

The iterative SENSE reconstruction was performed using the iGRASP implementation with a regularization weight of $\lambda = 0$. The reference CS reconstruction was performed separately for each coil element, followed by sensitivity-weighted combination. The regularization parameter was selected only once, as described for iGRASP.

To demonstrate the flexibility of iGRASP, reconstructions were also performed with different temporal resolutions for one of the pediatric datasets (13 and 34 spokes, corresponding to 3 and 8 s/volume).

Image reconstruction was performed using the C++ implementation on a Linux server equipped with four Intel Xeon E5520 quad core CPUs at 2.27 GHz and 96 GB of RAM. The reconstruction time ranged from 30 to 45 min for a complete 3D data set, depending on the size of datasets.

Image Analysis and Statistics

To evaluate the image quality and temporal fidelity achieved with iGRASP, one representative partition was selected from each reconstructed dataset for image quality assessment. Images were compared between iGRASP versus iterative SENSE, iGRASP versus coil-by-coil CS, and for temporal fidelity assessment between iGRASP versus NUFFT.

Image Quality Assessment

A total of 39 liver datasets (13 iterative SENSE, 13 coil-by-coil CS and 13 iGRASP), 15 pediatrics datasets (5 iterative SENSE, 5 coil-by-coil CS and 5 iGRASP), 18 breast datasets (6 iterative SENSE, 6 coil-by-coil CS and 6 iGRASP), and 30 neck datasets (10 iterative SENSE, 10 coil-by-coil CS and 10 iGRASP) were pooled and randomized for blinded qualitative evaluation by three radiologists with expertise on abdominal imaging, breast imaging and neuroimaging, respectively. The score levels for all the image quality assessments were: 1 = nondiagnostic, 2 = poor, 3 = adequate, 4 = good, and 5 = excellent.

The reported scores in each reconstruction category from all four applications were pooled together to represent mean ± standard deviation. Wilcoxon signed-rank sum test was chosen to compare the scores between iGRASP versus iterative SENSE and iGRASP versus coil-by-coil CS (n = 34), using Excel (Microsoft, Redmond, WA) where $P < 0.05$ was considered to be statistically significant difference.

Temporal Fidelity Assessment

For each of the iGRASP datasets, a ROI was manually drawn to evaluate the signal-intensity time courses. The upslope was computed using a linear fit of the curve points chosen between 10% and 90% of the relative peak enhancement, which usually corresponded to the first pass of contrast agent. The corresponding NUFFT data set was evaluated using the same ROI, and the upslope was calculated using the same length of curve points as reference. The analysis was performed on all iGRASP datasets (n = 34) and the corresponding NUFFT results. The upslope of NUFFT and iGRASP reconstructions were pooled separately and the relative accuracy was evaluated by performing linear correlation and Intraclass correlation (ICC) in Excel (Microsoft, Redmond, WA).

RESULTS

Selection of Reconstruction Parameters

Figure 3 shows the results from the NUFFT reconstruction of one DCE liver data set (Fig. 3a) and the iGRASP reconstructions with three representative values of the weighting parameter λ (Fig. 3b–d). It should be noted that although the dynamic curves from the NUFFT reconstruction are contaminated by streaking artifacts, they still preserve good contrast-time evolution due to the fact that intensities were averaged over a relatively large ROI. Therefore, it can be used as a first rough measure to assess temporal fidelity. The results suggest that $\lambda = M_0*0.05$ yields a good balance between image quality and temporal fidelity (Fig. 3c). Higher weighting (Fig. 3d, $\lambda = M_0*0.09$) produces lower residual artifact and slightly better image quality but also stronger temporal blurring, and vice versa for a lower weight (Fig. 3b, $\lambda = M_0*0.01$). Based upon these results, $\lambda = M_0*0.05$ was selected by the radiologist for iGRASP reconstructions with 21 spokes. As shown in the following sections, this weight led to similarly good results in other applications.

iGRASP versus Coil-by-Coil Compressed Sensing and Iterative SENSE

Figure 4 shows the comparison of iGRASP with coil-by-coil CS and iterative SENSE reconstructions for a liver dataset with in-plane matrix size of 384 × 384. iGRASP showed better image quality than coil-by-coil CS reconstruction, largely as a result of the reduction of aliasing artifacts provided by the parallel-imaging component (Fig. 1b). The reduction of aliasing artifacts enabled recovery of more signal coefficients, particularly those corresponding to high resolution features, which generally have lower values. iGRASP also outperformed iterative SENSE and showed significantly lower residual aliasing artifacts due to the temporal TV constraint, which exploits additional temporal correlation and sparsity.

Dynamic Pediatric Body Imaging

Figure 5a shows one representative partition of DCE-MRI from a 10-year old patient. The reconstructed images clearly show distinct aorta, portal vein, and liver contrast enhancement over time. Note that the same dataset was used to reconstruct dynamic images with different temporal resolutions by grouping 34 (top), 21 (middle), and 13 (bottom) spokes. Figure 5b evaluates the corresponding signal intensity changes over time for the aorta (AO) and portal vein (PV). For comparison, the signal intensity-time curves of the NUFFT reconstruction are included as reference.

Dynamic Breast Imaging

Figure 6a shows unilateral breast DCE-MRI of a patient with fibroadenoma and fibrocystic changes. The images
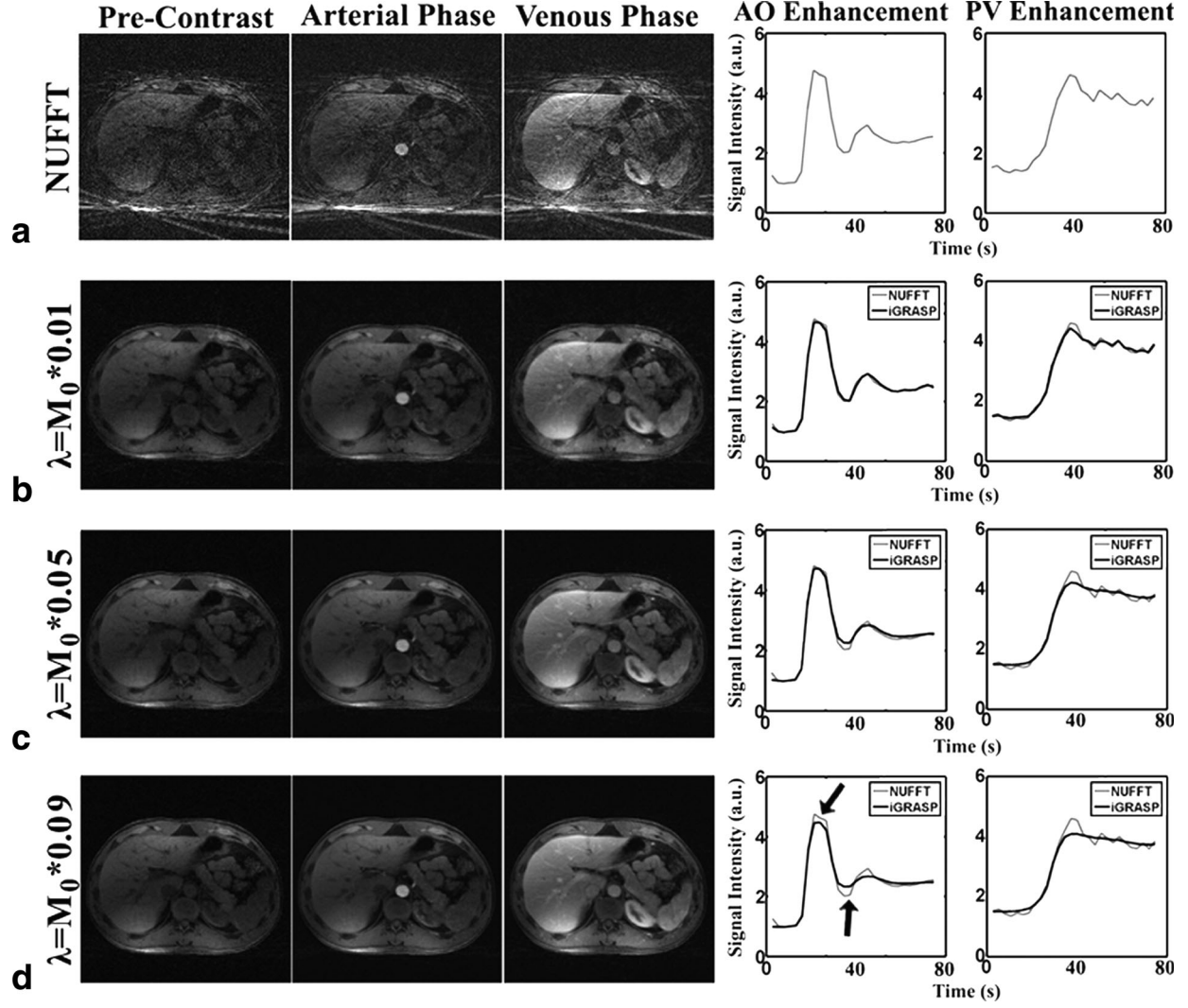
FIG. 3. Reconstruction of one representative partition from the contrast-enhanced volumetric liver dataset acquired with golden-angle radial sampling scheme using NUFFT (**a**) and iGRASP with three different weighting parameters (**b–d**) by grouping 21 consecutive spokes in each temporal frame. Results with $\lambda = M_0$*0.05 achieved an appropriate compromise between image quality and temporal fidelity. This value was therefore chosen for iGRASP reconstruction with temporal resolutions of 21 spokes per frame. The weighting parameter was adjusted for different temporal resolutions according to the level of incoherent aliasing artifacts or pseudo-noise in the PSF. M_0 was the maximal magnitude value of the NUFFT images that were also used to initialize the iGRASP reconstruction.

reconstructed with iGRASP show appropriate contrast enhancement over time in the normal breast tissue and in a suspicious breast lesion indicated by the white arrow. iGRASP also provided good image quality and depiction of relevant morphological features, such as fibroglandular tissue, skin layer, and the suspicious lesion. Figure 6b shows the corresponding signal intensity changes over time of the breast lesion, heart cavity, vessel and breast tissue (white arrows and ROI). The iGRASP reconstruction did not introduce significant notable temporal blurring.

Dynamic Neck Imaging

Figure 7 shows representative images of two partitions from a patient with neck mass and squamous cell cancer, together with the corresponding signal-intensity changes for the carotid artery (white arrows). The reconstruction

shows good image quality in different phases and similar contrast enhancement to the NUFFT curves.

Image Quality Comparison

Table 2 summarizes the mean scores and standard deviations for different reconstruction strategies in each application. iGRASP yielded significantly better scores ($P < 0.05$) when compared with both iterative SENSE and coil-by-coil CS reconstructions. The score of iGRASP was above 3.0 in all applications, suggesting that good image quality can be achieved with the proposed acceleration rate and temporal resolution.

Temporal Fidelity Comparison

For the upslope calculated from the data pairs (n = 34, iGRASP versus NUFFT), the linear regression coefficient
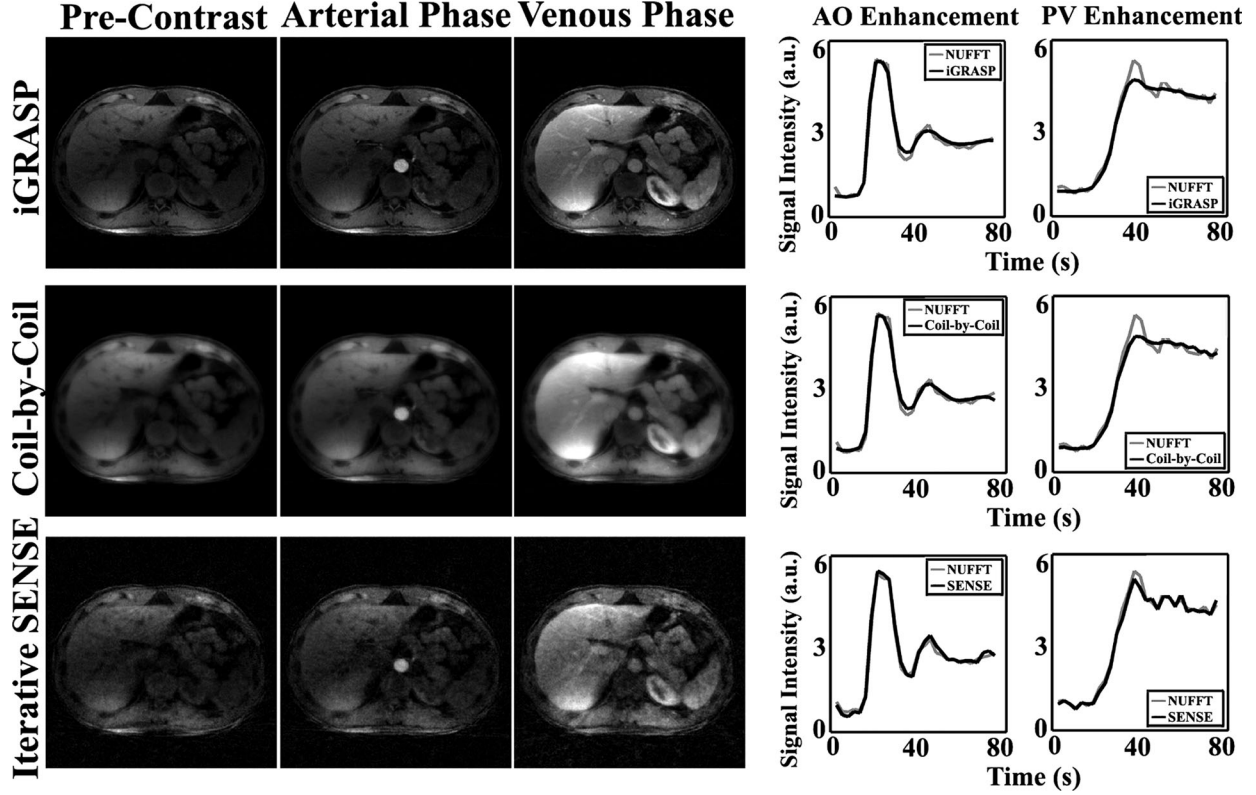
FIG. 4. Comparison of iGRASP (top) reconstruction with coil-by-coil CS (middle) and iterative SENSE (bottom) reconstructions in the liver dataset with the same acceleration rate and temporal resolution of 21 spokes/frame = 3 s/volume. iGRASP showed superior image quality compared with both coil-by-coil CS and iterative SENSE reconstructions.

was 0.99, the linear fitting slope was 0.98, and ICC was 0.99, indicating strong agreement between the upslopes obtained from iGRASP and NUFFT. This result suggests that iGRASP does not introduce significant temporal blurring.

DISCUSSION

This work introduces a robust approach for rapid dynamic volumetric MRI named iGRASP, which is applicable for a broad spectrum of clinical applications. Even though individual components of the method have been proposed before, the synergistic combination of CS, PI, and golden-angle radial sampling results in a technique that is particularly well-suited to obtain high spatial resolution, high temporal resolution, and large volumetric coverage at the same time. iGRASP achieved significantly better performance than either PI or CS alone and demonstrated high value for clinical studies that require robustness to patient motion and simultaneous high spatial and temporal resolution. iGRASP can be also used in other applications such as cardiac cine imaging (39).

The motion robustness can be mainly attributed to the use of radial k-space sampling. Radial sampling is well-known for being less susceptible than Cartesian sampling due to (a) lower sensitivity to motion-induced phase shifts and (b) signal averaging at the center of k-space. Moreover, it is well-suited for CS because radial undersampling creates incoherent low-intensity streaking artifacts. The

golden-angle ordering scheme additionally introduces temporal incoherence of the k-space acquisition.

In radial acquisitions, the image contrast corresponds to the average over the acquisition window because all lines cover k-space center. In this regard, radial sampling introduces a certain amount of temporal blurring, which manifests as slightly lower vessel-tissue contrast compared with Cartesian acquisitions that use a narrow time window for the acquisition of the k-space center. However, as opposed to other radial approaches that use a broad temporal view-sharing filter to extract different temporal phases without streaking artifacts (28), iGRASP enforces data fidelity only within a relatively small temporal window (e.g., 21 spokes), which enables to preserve high temporal sharpness.

iGRASP reconstruction removes streaking artifacts in the undersampled time-series of images at the expense of suppressing small coefficients in the temporal TV domain, which can compromise temporal fidelity for high acceleration factors because rapidly oscillating intensity changes may be dampened in this case while the temporal onset of sharp intensity changes remains unaffected due to the use of the l_1 norm. However, unlike reconstruction approaches that use TV constrains in the spatial domain, iGRASP does not lead to spatial image blurring or synthetic appearance. In cases where there is motion between temporal frames, temporal blurring artifacts might under certain circumstances appear as spatial blurring artifacts, but these artifacts originate in the temporal dimension. This penalty, which is
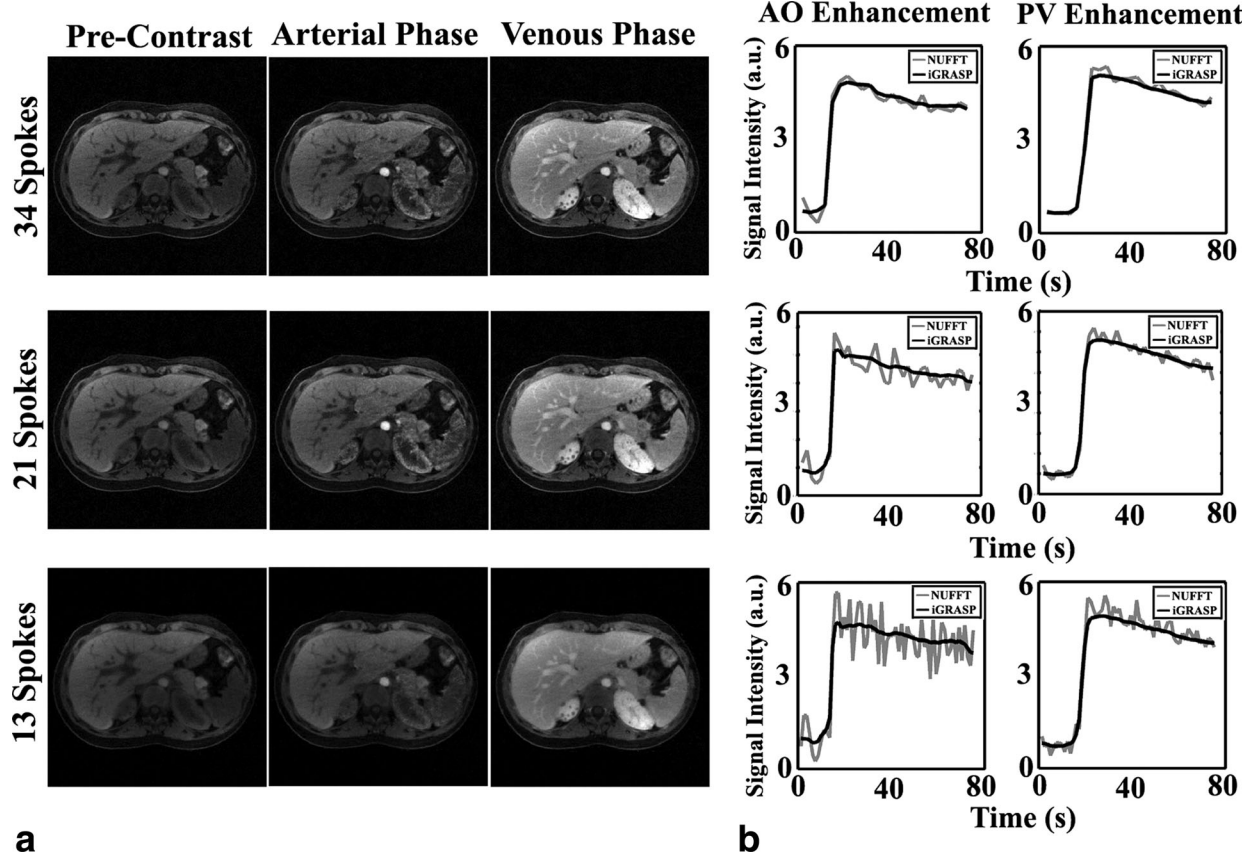
FIG. 5. a: iGRASP reconstruction of free-breathing contrast-enhanced volumetric abdominal imaging of a 10-year old patient referred for tuberous sclerosis. Representative images with three different temporal resolutions are shown, including (top) 34 spokes/frame = 8 s/volume, (middle) 21 spokes/frame = 5 s/volume and (bottom) 13 spokes/frame = 3 s/volume. The reconstructed image matrix size was 256 × 256 in each dynamic frame, with in-plane spatial resolution of 1 mm and the weighting parameters of different temporal resolutions were adjusted according to the acceleration rate. **b:** Signal-intensity time courses for the aorta and portal vein, which do not show significant temporal blurring as compared with the corresponding NUFFT results.
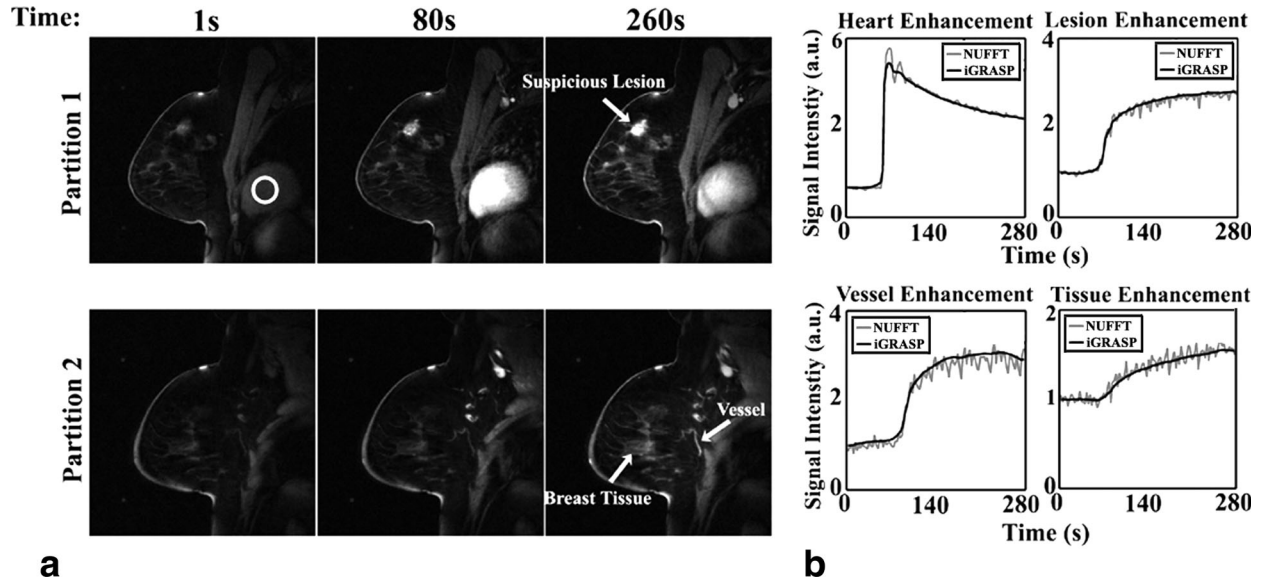

FIG. 6. a: iGRASP reconstruction of free-breathing contrast-enhanced volumetric unilateral breast imaging in an adult patient with fibroadenoma and fibrocystic changes. Temporal resolution is 21 spokes/frame = 3 s/volume. The reconstructed image matrix size is 256 × 256 for each dynamic frame, with in-plane spatial resolution of 1.1 mm. **b:** Signal-intensity time courses for the breast lesion, which is a fibroadenoma with fibrocystic changes (white arrow), for the heart cavity (white ROI), and for a blood vessel and breast tissue (white arrows), showing no significant temporal blurring.
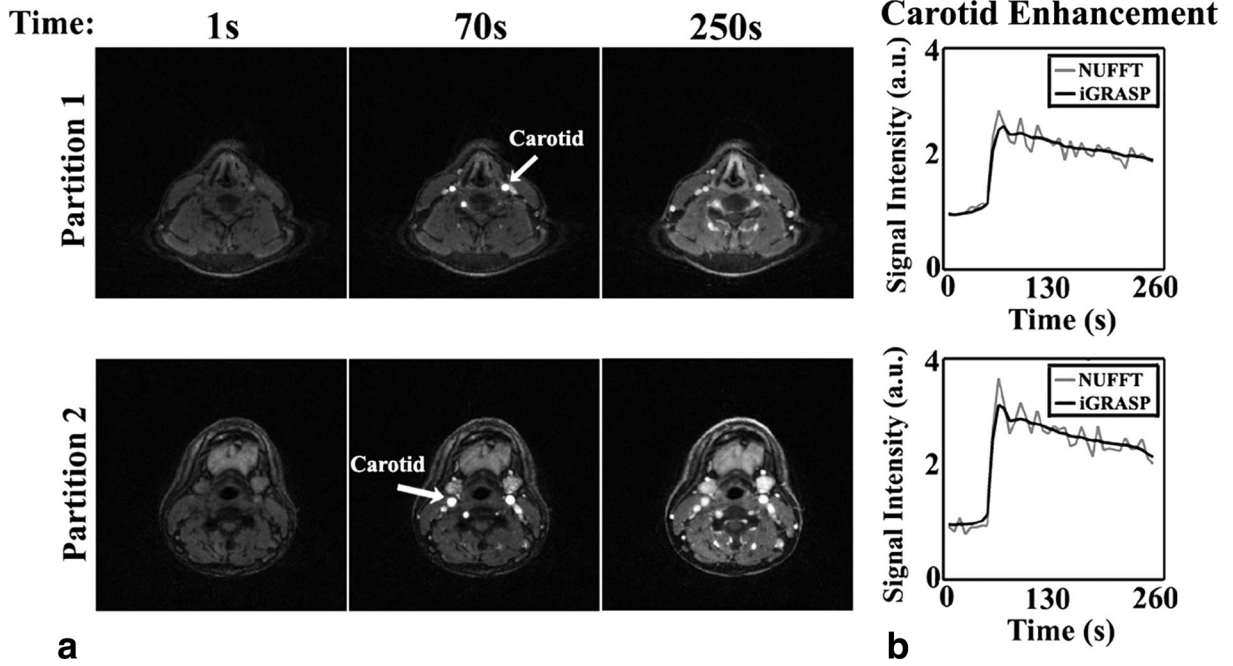
FIG. 7. a: iGRASP reconstruction of contrast-enhanced volumetric neck imaging in an adult patient with neck mass and squamous cell cancer. Temporal resolution is 21 spokes/frame = 7 s/volume. The reconstructed image matrix size is 256 × 256 for each dynamic frame, with in-plane spatial resolution of 1 mm. **b:** Signal-intensity time courses evaluated for the carotid arteries show no significant temporal blurring.

common to all compressed sensing methods, is due to the fact that MR images are compressible rather than truly sparse, presenting a few high coefficients and many small coefficients. If the small coefficients fall below the pseudo-noise level created by the undersampling artifacts, they may not be robustly recoverable. For the particular case of temporal TV, abrupt temporal variations usually result in high coefficients that are well recovered by the reconstruction. However, moderate or smooth signal variations might result in low-value coefficients below the pseudo-noise level, which could be suppressed by the reconstruction. Although minor compromises in the temporal fidelity may result, it is unclear whether these effects are clinically relevant. Future studies are planned to assess the impact on the diagnostic performance of dynamic imaging, although the preliminary results obtained so far indicate that the technique does not introduce clinically significant temporal distortions. From a clinical perspective, it is presumably of higher relevance that iGRASP enables dynamic abdominal imaging in patients that are incapable of suspended respiration, including severely sick, pediatric, or sedated patients, where it is infeasible to perform dynamic imaging with adequate diagnostic quality using established conventional techniques (40,41).

iGRASP provides a simple and flexible way of performing dynamic MRI studies in these patients and can help to improve clinical workflow by enabling data acquisition without the need for synchronization with breath-hold commands or for selection of a predefined rigid temporal resolution. While a typical clinical use case does not require reconstruction and evaluation of image series at multiple temporal resolutions, which would increase the workload of radiologists if used indiscriminately, the flexibility of reconstructing different temporal resolutions without the need to re-acquire data can be another advantage for specific clinical questions or in the event of a suggestive finding. Formal studies are currently in progress using a prototypic workflow integration (42) to investigate the clinical potential of multi-resolution reconstructions and to determine the range of effectively achievable temporal resolutions.

The current implementation of iGRASP has some limitations that will be addressed in future work. First, a stack-of-stars k-space sampling pattern is used to enable parallelized slice-by-slice reconstructions. This reduces the computational burden of iGRASP reconstructions, but prevents using compressed sensing along the slice dimension. The use of full 3D golden-angle radial sampling along with a volumetric reconstruction are

Table 2

Image Quality Assessment Scores Represent Mean ± Standard Deviation For Each Reconstruction Category For Different Applications

	DCE Liver	DCE Pediatrics	DCE Breast	DCE Neck
iGRASP	3.38±0.65	4.20±0.84	4.67±0.52	3.80±0.79
Coil-by coil CS	1.62±0.77	1.80±0.45	2.33±1.03	2.10±0.74
Iterative SENSE	1.38±0.65	1.40±0.55	2.17±1.17	1.00±0.00

expected to further increase the performance, at the expense of higher computational demand. Second, although temporal TV has been used before for different dynamic MRI reconstructions and was shown to be better in some specific applications (19), it may be not optimal to use it as the only sparsifying transform for all cases and applications. Other advanced temporal sparsifying transforms, such as dictionary learning, might be also useful to increase temporal fidelity for high undersampling factors. Third, the current work did not use rigorous mathematical criteria to select the weighting parameter λ, which controls the tradeoff between removal of streaking aliasing artifacts and temporal fidelity. The empirical rule to make λ proportional to the pseudo-noise level in the PSF produced reasonable performance for different undersampling factors. The same λ was also used in different applications for a given temporal resolution, which suggests that the reconstruction can be automated without intervention. However, evaluation on a larger set of patients comparing with standard clinical techniques is required to test the robustness of this new approach. Finally, because it is impossible in practice to acquire a fully-sampled volumetric DCE dataset with the target spatial and temporal resolution, the current study used NUFFT reconstructions as temporal reference. While NUFFT reconstructions provide time curves without artificial temporal blurring effects, they can be affected by strong streaking artifacts at high accelerations that limit their value for assessing the ground-truth signal evolution. A comprehensive analysis of the temporal fidelity achieved with iGRASP using numerical simulations and dynamic phantom scans is currently in progress.

CONCLUSIONS

The combination of compressed sensing, parallel imaging, and golden-angle radial sampling used in iGRASP enables rapid dynamic volumetric MRI studies with high spatial resolution, temporal resolution, and motion robustness. Because of the continuous data acquisition and the flexibility to reconstruct images retrospectively at different temporal resolutions, dynamic imaging with iGRASP can be integrated easily into clinical workflow (42). iGRASP can be used for a wide range of clinical applications and demonstrated particular value for examinations of patients that are unable to suspend respiration.

ACKNOWLEDGMENTS

REFERENCES

1. Padhani AR. Dynamic contrast-enhanced MRI in clinical oncology: current status and future directions. J Magn Reson Imaging 2002;16: 407–422.
2. Xu B, Spincemaille P, Chen G, Agrawal M, Nguyen TD, Prince MR, Wang Y. Fast 3D contrast enhanced MRI of the liver using temporal resolution acceleration with constrained evolution reconstruction. Magn Reson Med 2013;69:370–381.
3. Sodickson DK, Manning WJ. Simultaneous acquisition of spatial harmonics (SMASH): fast imaging with radiofrequency coil arrays. Magn Reson Med 1997;38:591–603.
4. Pruessmann KP, Weiger M, Scheidegger MB, Boesiger P. SENSE: sensitivity encoding for fast MRI. Magn Reson Med 1999;42:952–962.
5. Griswold MA, Jakob PM, Heidemann RM, Nittka M, Jellus V, Wang J, Kiefer B, Haase A. Generalized autocalibrating partially parallel acquisitions (GRAPPA). Magn Reson Med 2002;47:1202–1210.
6. Kellman P, Epstein FH, McVeigh ER. Adaptive sensitivity encoding incorporating temporal filtering (TSENSE). Magn Reson Med 2001;45: 846–852.
7. Breuer FA, Kellman P, Griswold MA, Jakob PM. Dynamic autocalibrated parallel imaging using temporal GRAPPA (TGRAPPA). Magn Reson Med 2005;53:981–985.
8. Tsao J, Kozerke S. MRI temporal acceleration techniques. J Magn Reson Imaging 2012;36:543–560.
9. Tsao J, Boesiger P, Pruessmann KP. k-t BLAST and k-t SENSE: dynamic MRI with high frame rate exploiting spatiotemporal correlations. Magn Reson Med 2003;50:1031–1042.
10. Huang F, Akao J, Vijayakumar S, Duensing GR, Limkeman M. k-t GRAPPA: a k-space implementation for dynamic MRI with high reduction factor. Magn Reson Med 2005;54:1172–1184.
11. Xu D, King KF, Liang ZP. Improving k-t SENSE by adaptive regularization. Magn Reson Med 2007;57:918–930.
12. van Vaals JJ, Brummer ME, Dixon WT, Tuithof HH, Engels H, Nelson RC, Gerety BM, Chezmar JL, den Boer JA. "Keyhole" method for accelerating imaging of contrast agent uptake. J Magn Reson Imaging 1993;3:671–675.
13. Jones RA, Haraldseth O, Muller TB, Rinck PA, Oksendal AN. K-space substitution: a novel dynamic imaging technique. Magn Reson Med 1993;29:830–834.
14. Candes E, Romberg JT. Robust uncertainty principles: exact signal reconstruction from highly incomplete frequency information. IEEE Trans Inf Theory 2006;52:489–509.
15. Donoho D. Compressed sensing. IEEE Trans Inf Theory 2006;52: 1289–1306.
16. Lustig M, Donoho D, Pauly JM. Sparse MRI: the application of compressed sensing for rapid MR imaging. Magn Reson Med 2007;58: 1182–1195.
17. Lustig M, Santos J, Donoho D, Pauly J. k-t SPARSE: high frame rate dynamic MRI exploiting spatio-temporal sparsity. In Proceedings of the 14th Annual Meeting of ISMRM, Seattle, Washington, USA, 2006. p. 2420.
18. Gamper U, Boesiger P, Kozerke S. Compressed sensing in dynamic MRI. Magn Reson Med 2008;59:365–373.
19. Adluru G, Awate SP, Tasdizen T, Whitaker RT, Dibella EV. Temporally constrained reconstruction of dynamic cardiac perfusion MRI. Magn Reson Med 2007;57:1027–1036.
20. Jung H, Sung K, Nayak KS, Kim EY, Ye JC. k-t FOCUSS: a general compressed sensing framework for high resolution dynamic MRI. Magn Reson Med 2009;61:103–116.
21. Otazo R, Kim D, Axel L, Sodickson DK. Combination of compressed sensing and parallel imaging for highly accelerated first-pass cardiac perfusion MRI. Magn Reson Med 2010;64:767–776.
22. Feng L, Otazo R, Jung H, Jensen JH, Ye JC, Sodickson DK, Kim D. Accelerated cardiac T2 mapping using breath-hold multiecho fast spin-echo pulse sequence with k-t FOCUSS. Magn Reson Med 2011; 65:1661–1669.
23. Kim D, Dyvorne HA, Otazo R, Feng L, Sodickson DK, Lee VS. Accelerated phase-contrast cine MRI using k-t SPARSE-SENSE. Magn Reson Med 2012;67:1054–1064.
24. Feng L, Srichai MB, Lim RP, Harrison A, King W, Adluru G, Dibella EV, Sodickson DK, Otazo R, Kim D. Highly accelerated real-time cardiac cine MRI using k-t SPARSE-SENSE. Magn Reson Med 2013;70: 64–74.
25. Block KT, Uecker M, Frahm J. Undersampled radial MRI with multiple coils. Iterative image reconstruction using a total variation constraint. Magn Reson Med 2007;57:1086–1098.
26. Glover GH, Pauly JM. Projection reconstruction techniques for reduction of motion effects in MRI. Magn Reson Med 1992;28:275–289.
27. Gai N, Axel L. Correction of motion artifacts in linogram and projection reconstruction MRI using geometry and consistency constraints. Med Phys 1996;23:251–262.

28. Winkelmann S, Schaeffter T, Koehler T, Eggers H, Doessel O. An optimal radial profile order based on the Golden Ratio for time-resolved MRI. IEEE Trans Med Imaging 2007;26:68–76.

29. Chan RW, Ramsay EA, Cheung EY, Plewes DB. The influence of radial undersampling schemes on compressed sensing reconstruction in breast MRI. Magn Reson Med 2012;67:363–377.

30. Usman M, Atkinson D, Odille F, Kolbitsch C, Vaillant G, Schaeffter T, Batchelor P, Prieto C. Motion corrected compressed sensing for free-breathing dynamic cardiac MRI. Magn Reson Med 2012. doi: 10.1002/mrm.24463.

31. Hansen MS, Sorensen TS, Arai AE, Kellman P. Retrospective reconstruction of high temporal resolution cine images from real-time MRI using iterative motion correction. Magn Reson Med 2012;68: 741–750.

32. Prieto C, Uribe S, Razavi R, Atkinson D, Schaeffter T. 3D undersampled golden-radial phase encoding for DCE-MRA using inherently regularized iterative SENSE. Magn Reson Med 2010;64: 514–526.

33. Walsh DO, Gmitro AF, Marcellin MW. Adaptive reconstruction of phased array MR imagery. Magn Reson Med 2000;43:682–690.

34. Griswold MA WD, Heidemann RM, Haase A, Jakob PM. The use of an adaptive reconstruction for array coil sensitivity mapping and intensity normalization. In Proceedings of the 10th Annual Meeting of ISMRM, Honolulu, Hawaii, USA, 2002. Abstract 2410.

35. Buehrer M, Pruessmann KP, Boesiger P, Kozerke S. Array compression for MRI with large coil arrays. Magn Reson Med 2007;57:1131–1139.

36. Dagum L, Open MP. An industry standard API for shared-memory programming. IEEE Comput Sci Eng 1998;5:46–55.

37. Nocedal J. Updating quasi-Newton matrices with limited storage. Math Comput 1980;35:773–782.

38. Block KT, Uecker M. Simple method for adaptive gradient-delay compensation in radial MRI. In Proceedings of the 19th Annual Meeting of ISMRM, Montreal, Canada, 2011. p. 2816.

39. Feng L, Xu J, Axel L, Sodickson DK, Otazo R. High spatial and temporal resolution 2D real time and 3D whole-heart cardiac cine MRI using compressed sensing and parallel imaging with golden angle radial trajectory. In Proceedings of the 20th Annual Meeting of ISMRM, Melbourne, Australia, 2012. p. 225.

40. Chandarana H, Block TK, Rosenkrantz AB, Lim RP, Kim D, Mossa DJ, Babb JS, Kiefer B, Lee VS. Free-breathing radial 3D fat-suppressed T1-weighted gradient echo sequence: a viable alternative for contrast-enhanced liver imaging in patients unable to suspend respiration. Invest Radiol 2011;46:648–653.

41. Chandarana H, Feng L, Block KT, Rosenkrantz AB, Lim P, Babb J, Sodickson DK, Otazo R. Free-breathing contrast-enhanced multiphase MRI of the liver using a combination of compressed sensing, parallel imaging, and golden-angle radial sampling. Invest Radiol 2013;48:10–16.

42. Block KT, Grimm R, Feng L, Otazo R, Chandarana H, Bruno M, Sodickson DK. Bringing compressed sensing to clinical reality: prototypic setup for evaluation in routine applications. In Proceedings of the 21st Annual Meeting of ISMRM, Salt Lake City, Utah, USA 2013. p. 3809.